ORIGINAL ARTICLE

Ionospheric delay corrections for single-frequency GPS receivers over Europe using tomographic mapping

Damien J. Allain · Cathryn N. Mitchell

Abstract The majority of navigation satellites receivers operate on a single frequency and experience a positioning error due to the ionospheric delay. This can be compensated for using a variety of approaches that are compared in this paper. The study focuses on the last solar maximum. A 4D tomographic imaging technique is used to map the ionospheric electron density over the European region during 2002 and 2003. The electron density maps are then used to calculate the excess propagation delay on the L1 frequency experienced by GPS receivers at selected locations across Europe. The excess delay is applied to correct the pseudo-range single frequency observations at each location and the improvements to the resulting positioning are calculated. The real-time tomographic technique is shown to give navigation solutions that are better than empirical modelling methods and approach the accuracy of the full dual-frequency solution. The improvements in positioning accuracy vary from day to day depending on ionospheric conditions but can be up to 25 m during mid-day during these solar maximum conditions at European mid-latitudes.

Keywords Ionosphere · GPS

D. J. Allain (✉) · C. N. Mitchell
Department of Electronic and Electrical Engineering,
University of Bath, Bath BA2 7AY, UK
e-mail: D.Allain@bath.ac.uk

Introduction

The largest single source of positioning error to single-frequency Global Positioning System (GPS) receivers is due to the unknown excess delay of the signal as it propagates through the ionosphere. There are two methods to compensate for the delay. The first is to use a model that represents the expected ionospheric delay, for example the Klobuchar (1987) model or the International Reference Ionosphere (IRI) model (Bilitza 2001). An alternative approach is to implement real-time mapping and to transmit this information to the navigation user.

The idea to map the ionosphere in real time to make corrections has been studied and implemented in various regions of the world. The Wide Area Augmentation System (WAAS) is available in North America, European Geostationary Navigation Overlay System (EGNOS) is the European system, while Multi-functional Satellite Augmentation System (MSAS) operates in Asia. In the case of the Klobuchar (1987) model the ionospheric information is sent on the navigation satellite signals, whereas for the real-time mapping the information is sent regionally via a geostationary satellite broadcasting on GPS frequencies. Such real-time mapping systems are expected to offer greater accuracy over models but they do require infrastructure in the form of a network of dual-frequency receivers over the area of interest. Each of the current real-time ionospheric correction systems uses the concept of approximating the ionosphere to a delay at a single height in the ionosphere (thin shell model). An alternative concept, tomographic imaging, is a medical imaging technique to create images of a parameter from integrated measurements. It is useful for ionospheric mapping because it allows the depth field of the object to be correctly represented; the ionosphere has a depth of several hundred

kilometres. The representation of the ionospheric delay in the form of electron density images allows more accurate calculation of the slant delay from a particular location than is possible from a shell approximation (Meggs and Mitchell 2006). A comprehensive review of ionospheric imaging is given by Bust and Mitchell (2008). Ionospheric mapping has already successfully been used for dual frequency GPS carrier-phase positioning over long baselines (Hernández-Pajares et al. 2000).

The aim of this paper is to test the navigation accuracy that could be achieved using tomographic images of electron density to correct for the unknown excess delay on single frequency signals. This is demonstrated through a series of comparisons between navigation calculations that are each performed using a different approach to the ionospheric corrections: (1) no correction (2) Klobuchar model (3) IRI model (4) forecast imaging (5) near-real-time imaging (6) dual frequency receiver. The distinction between the forecast and the near real time imaging is to compare different latencies to allow for the data collation, calculations and transmission essential for the implementation of a correction system. The dual-frequency result is a benchmark that shows the best position that can be achieved at that instant without time averaging.

Method

This study covers several days: all the days of 2002 and from 21 October to 4 November 2003, showing diurnal and seasonal changes over a solar maximum year and a major storm period.

GPS receivers from four different sites in mainland Europe were used to test the six different methods. Each receiver recorded dual frequency data in Receiver Independent Exchange Format (RINEX) format at a sampling period of 30 s. This is much longer than the 1 s sampling period normally used for real-time positioning but is sufficient to compare the ionospheric corrections. The locations of these test sites are shown as red × marks in Fig. 1. The green + marks in Fig. 1 show the locations of dual frequency GPS receivers that were used in the tomographic imaging to create the ionospheric corrections for methods 4 and 5.

The satellite positions were calculated from the precise ephemerides obtained from the International GNSS Service (IGS). These were interpolated using a four-harmonic interpolation applied to 2-h of the orbit to achieve an accuracy of 0.25 m in the satellite position. Satellite specific clock biases were obtained from the IGS and linear interpolation was used to estimate their values at the appropriate times. In order to implement calculations for the single-frequency positioning with no ionospheric
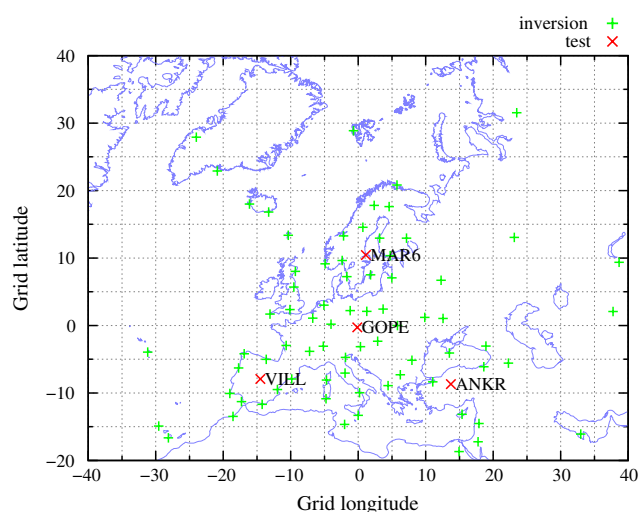

Fig. 1 Location of the test sites (×) and sites used for imaging (+)

correction the P1 code was extracted from the RINEX file. Corrections were made for the Sagnac effect and the satellite relativistic clock bias in accordance with Ashby and Spilker (1995). The tropospheric delays were estimated from receiver altitude and satellite elevation using the approach of Spilker (1994). These corrections resulted in a set of partially corrected pseudorange observations for each site at the sample rate of the IGS data, 30 s. The receiver position was then calculated using a least-squares estimate applied to the corrected pseudorange observations. At this stage no account was taken of the ionosphere and thus this constituted the first method, the results of which are labelled 'uncorrected'. The five remaining approaches, each accounting for the ionosphere are now described below.

The second method was to use the Klobuchar model, currently broadcast in the form of coefficients over the GPS L1 signal. The model represents the global ionosphere into eight coefficients that can be used by a receiver based algorithm to make real-time corrections to the signal pseudoranges. The results from this model are labelled 'Klobuchar'. The third method was to use the IRI 2001 model (labelled 'IRI2001'). This provides a full 3D description of the electron density on a global scale assuming knowledge of the date, time and solar output. This model is not currently used for GPS ionospheric corrections on a real-time basis although it could be applied to the system if the model were embedded into a GPS receiver and coefficients were broadcast. The ionospheric corrections were calculated using a forward integration through the model along slant paths to estimate the ionospheric delay to the L1 signal. The fourth method was to use a real-time mapping tomographic algorithm known as Multi Instrument Data Analysis System (MIDAS). The version of the algorithm described in

Mitchell and Spencer (2003) was implemented here with upgrades described in Spencer and Mitchell (2007). The input data came from dual frequency receivers. Their distribution across and around Europe, shown in Fig. 1, is representative of those available in near-real time. A forecast to real-time (up to 40 min ahead) was then implemented using algorithms described in Dear (2007). These results are labelled '40min forecast'. For further comparison a non-forecasted near-real-time result is shown, labelled 'near real-time'.

Ionospheric maps

The same grid was used for the IRI model, the MIDAS tomography and the 40 min forecast. The area of coverage was extended far beyond the boundaries of Europe to allow the calculation of the (TEC) even for low elevation rays. The grid was centered at 50°N 15°E, allowing for a similar pixel size and shape to cover the area of study (Spencer and Mitchell 2007). The ranges were in latitude from −44° to +44° (west to east) in steps of 4°, in longitude from −44° to +44° (south to north) in steps of 4° and in altitude from 100 to 1,500 km in steps of 50 km.

The vertical basis functions used for the MIDAS inversions were three empirical orthonormal functions computed from a range of Epstein functions. The inversions were stabilised with a set of regularisation factors preventing departure from a linear gradient.

Pseudoranges

Ionospheric delay

The notations used here follow from Mannucci et al. (1999).

Klobuchar (1996) derives $I f^{-2}$ the ionospheric group delay or phase advance in metres, with f the frequency of the signal in hertz, $\int N \, dl$ the TEC in electrons per square meter, and I the ionospheric delay term in meter per square second:

$$I f^{-2} = 40.3 f^{-2} \int N \, dl \qquad (1a)$$

$$\text{or} \quad I = 40.3 \int N \, dl \qquad (1b)$$

Equation 1a shows the ionospheric delay can be calculated if the TEC is known, or measured if pseudorange observations are available for at least two frequencies.

The dual-frequency position is computed from ionosphere-free pseudoranges, here called P_0. It is itself computed from four observables P_1, P_2, L_1 and L_2 as explained below.

P_1 and P_2 are the pseudoranges from the precise P-code. L_1 and L_2 are the recorded carrier phases of the signal converted to distance units. Expressing P_1 and P_2 with P_0, $I f^{-2}$ and ϵ the noise:

$$P_1 = P_0 + I f_1^{-2} + \epsilon_1 \qquad (2a)$$

$$P_2 = P_0 + I f_2^{-2} + \epsilon_2 \qquad (2b)$$

and expressing L_1 and L_2 with P_0, $I f^{-2}$, n the integer ambiguity and λ the carrier wavelength:

$$L_1 = P_0 - I f_1^{-2} + n_1 \lambda_1 \qquad (3a)$$

$$L_2 = P_0 - I f_2^{-2} + n_2 \lambda_2 \qquad (3b)$$

gives two expressions for I:

$$\frac{P_1 - P_2}{f_1^{-2} - f_2^{-2}} = I + \frac{\epsilon_1 - \epsilon_2}{f_1^{-2} - f_2^{-2}} \qquad (4a)$$

$$\frac{L_1 - L_2}{f_1^{-2} - f_2^{-2}} = -I + \frac{n_1 \lambda_1 - n_2 \lambda_2}{f_1^{-2} - f_2^{-2}} \qquad (4b)$$

Equation 4a gives I with a noise term. Equation 4b gives I with an offset term from the integer ambiguity. The integer ambiguity stays constant while the satellite is visible apart from large and sudden changes called cycle slips. The offset term of Eq. 4b depends on the integer ambiguity and stays also constant apart from similar changes. As the changes of the offset term of Eq. 4b are large and sudden, they are easily detectable. The offset between cycle slips is taken as a weighted mean of the differences between the first and second solutions above, i.e. the value of I is computed by fitting Eq. 4b into Eq. 4a. The cosecant of the elevation angles are used for the weights. This way, the weights are correlated with the signal to noise ratio (Klobuchar 1996). We are then left with:

$$P_1 - I f_1^{-2} = P_0 + \epsilon \qquad (5a)$$

$$L_1 + I f_1^{-2} = P_0 + n_1 \lambda_1 \qquad (5b)$$

Again, Eq. 5a gives P_0 with a noise term and Eq. 5b gives P_0 with an offset term. P_0 is, as above for I, computed by fitting Eq. 5b into Eq. 5a with a similar weighted mean.

The uncorrected position is computed using P_1.

The other positions are computed from ionosphere-corrected pseudoranges, here called P'_0, similarly to Eq. 2a:

$$P'_0 = P_1 - I f_1^{-2} \qquad (6)$$

The ionospheric delay term I is here calculated using Eq. 1b, with N the electron concentration from the model or the map and dl from the ray-path to voxel intersection.

Other delays and biases

The ionosphere-free pseudorange or ionosphere-corrected pseudorange or uncorrected pseudorange P is itself made

of other terms : r the geometric range, r_s the Sagnac bias, $\Delta_s t$ and $\Delta_r t$ the satellite and receiver clock biases, c the speed of light in vacuum and $T_{\phi,h}$ the tropospheric delay:

$$P \simeq r + r_s + c(\Delta_r t + \Delta_s t) + T_{\phi,h} \tag{7a}$$

$$\text{giving} \quad P^* = r + c\Delta_r t \simeq P - r_s - c\Delta_s t - T_{\phi,h} \tag{7b}$$

Equation 7b gives the absolute pseudorange P^* to put into the least squares pseudorange calculation of Eq. 26.

The Sagnac bias r_s is given by Ashby and Spilker (1995), with $\overrightarrow{\Omega}$ the rotation vector of the Earth, $\overrightarrow{S}$ the position vector of the satellite and $\overrightarrow{R}$ the position vector of the receiver :

$$r_s \simeq c^{-1}\overrightarrow{\Omega} \cdot \overrightarrow{S} \times \overrightarrow{R} \tag{8}$$

The tropospheric delay $T_{\phi,h}$ is approximated in Spilker (1994), taking $T_{\pi/2,0} \approx 2.44$ m the azimuth delay at sea level, h the altitude of the receiver and ϕ the elevation angle of the satellite:

$$T_{\phi,h} \simeq T_{\pi/2,0} \frac{1.0121 \times e^{-0.133 \times 10^{-3} h}}{\sin \phi + 0.0121} \tag{9}$$

The satellite clock bias $\Delta_s t$ is the sum (Kouba and Héroux 2001) of a satellite-specific error $\Delta_s' t$ and of the relativistic effects on satellites with an elliptic orbit $\Delta_s^r t$, with S the distance of the satellite to the center of the reference frame and $\dot{S}$ the rate of change of this distance, from Ashby and Spilker (1995):

$$c\Delta_s^r t = 2S\dot{S}c^{-1} \quad \text{giving :} \quad c\Delta_s t = c\Delta_s' t + 2S\dot{S}c^{-1} \tag{10}$$

Estimates for each of the satellite-specific errors $\Delta_s' t$ and for each of the satellites positions are calculated and made publicly available by the IGS (Dow et al. 2005). A linear interpolation from the IGS value gives the satellite-specific clock bias $\Delta_s' t$. The method to interpolate for the position of the satellite $\overrightarrow{S}$ and to obtain its velocity $\overrightarrow{\dot{S}}$ from the IGS ephemeris is explained in "Satellite position and velocity".

The satellites show a small P1 to P2 bias $\Delta_s^{1 \rightarrow 2} t$. This gives a different clock bias for each frequency. The IGS ephemeris contains the satellite clock bias for the dual frequency. This means that the single frequency clock bias $\Delta_s^1 t$ is offset from the dual frequency clock bias $\Delta_s t$, from Eqs. 4a and 5a:

$$\Delta_s^1 t = \Delta_s t + \frac{f_1^{-2}}{f_1^{-2} - f_2^{-2}} \Delta_s^{1 \rightarrow 2} t \tag{11}$$

Satellite position and velocity

Antenna offsets

The IGS ephemeris gives the position of the center of mass of the satellites S' (Kouba and Héroux 2001). The antenna offsets have been calculated by Schmid et al. (2007). Horizontal satellite antenna offsets $\Delta_h S$ are extremely complicated to take into account but they are up to ≤ 279 mm and their impact ΔR on the range is

$$\Delta R \leq R/S \times \Delta_h S \quad \text{giving} \quad \Delta R \leq 67 \text{ mm} \tag{12}$$

so can be neglected. Taking $\Delta_v S$ the vertical component of the antenna offset and $\overrightarrow{S'}$ the position of the center of mass of the satellites, we have $\overrightarrow{S}$ the position of the antenna such as:

$$\overrightarrow{S} \simeq \frac{S' - \Delta_v S}{S'}\overrightarrow{S'} \tag{13}$$

Time of transmission and trigonometric interpolation

The IGS ephemeris gives the position of the satellites in the Earth-Centered Earth-Fixed (ECEF) frame once every 15 min. The precise coordinates of the antenna at the time of transmission t_t must be then be interpolated from surrounding values from the ephemeris and from t_t. The time of transmission t_t is contained in the signal data but is not recorded explicitly in the RINEX file. Trigonometric interpolation was chosen and an iteration process is also carried out to find the time of transmission t_t.

Interpolation of orbits can be computed using polynomial interpolation or trigonometric interpolation. Schenewerk (2003) shows that trigonometric interpolation gives the most accurate results with the least coefficients. The spline method was found to give results in error of around 25 m RMS. Trigonometric interpolation with 4 harmonics in the ECEF frame:

$$\overrightarrow{S} \simeq \sum_{i=1}^{4} \overrightarrow{A_i} \cos i\Omega t + \overrightarrow{B_i} \sin i\Omega t \tag{14}$$

was found to give the best results with an uncertainty of around 0.04 m RMS with a maximum of 0.15 m.

The time of transmission can be calculated from t_r the time of reception, which is recorded in the RINEX file, and from $RS \equiv r$, the distance from the satellite S to the receiver R:

$$t_t = t_r - c^{-1} r \tag{15}$$

The range r can be calculated from the coordinates of the receiver R and from the coordinates of the satellite S. R is considered to be known, but S is not as it is a function of the transmission time t_t. Therefore, iteration is necessary to solve for the satellite position S. The speed of approach, i.e. the rate at which the distance between a satellite and a receiver changes, is $|\dot{r}| < 800$ m s^{-1}. The uncertainty on the range Δr has an influence on the uncertainty of the transmission time Δt_t:

$$\Delta t_t < c^{-1}\Delta r \tag{16}$$

and the uncertainty of the transmission time Δt_t has itself an influence on the uncertainty of the range Δr:

$$\Delta r = |\dot{r}|\Delta t_t \tag{17}$$

Each iteration then multiplies the uncertainty on the range by $c^{-1}|\dot{r}| < 2.7 \times 10^{-6}$. The computation therefore converges quickly toward the solution.

The range r between a satellite and a receiver is between 20.2×10^6 m and 26.6×10^6 m, or:

$$r = (23.4 \pm 3.2) \times 10^6 \tag{18}$$

The aim is to achieve an uncertainty of $\Delta r < 0.1$ m. This gives the number of iterations required:

$$\frac{\ln(0.1/3.2 \times 10^6)}{\ln(|\dot{r}|/c)} \le 2 \tag{19}$$

Two iterations are then carried out. They would reduce the range uncertainty to $3.2 \times 10^6 \times (c/\dot{r})^{-2} < 3 \times 10^{-5}$ m if it were not for the intrinsic inaccuracy of the interpolation methods. As trigonometric interpolation was found to be slow, the first interpolation was carried with a spline, which was found to be a much faster method. It would reduce the range uncertainty to $3.2 \times 10^6 \times c^{-1}\dot{r} < 9$ m if it were not for the intrinsic limitations of the spline interpolation. It would therefore require another iteration. It actually reduces the range uncertainty to 25 m RMS. The second interpolation would reduce the range uncertainty to $25 \times c^{-1}\dot{r} < 7 \times 10^{-5}$ m RMS which is much smaller than the intrinsic limitations of the trigonometric interpolation. Using this approach the satellite position is actually determined to within 0.15 m.

Satellite velocity

Numerical differentiation is slow because it requires the computation of two additional interpolations and is also subject to rounding errors. As an alternative, the coefficients found in the interpolation of the positions are multiplied by the derivatives of the trigonometric functions used in the interpolation of the positions, from Eq. 14:

$$\overrightarrow{\dot{S}} \simeq \sum_{i=1}^{4} i\Omega\left(-\overrightarrow{A_i}\sin i\Omega t + \overrightarrow{B_i}\cos i\Omega t\right) \tag{20}$$

This method is much more accurate and much faster than numerical differentiation.

The precise velocity and position of the satellite are then used to calculate the relativistic clock bias of the satellite $\Delta_s^r t$, in Eq. 10, and, with the position of the receiver, the Sagnac bias r_s, in Eq. 8.

Least squares

The following section draws from material found in Parkinson (1996).

Typically more than four satellites are visible to a receiver. In this case a least square fit of the solution is appropriate. For $n \ge 4$ satellites, taking a receiver of position R and a satellite of position S_i, with $1 \le i \le n$, the absolute pseudorange P^*_i is:

$$P_i^* = c\Delta_r t + r_i \tag{21}$$

Rewriting r_i with $\overrightarrow{r_i}$ the receiver to satellite vector, $\hat{r}_i$ its unit vector and $\overrightarrow{S_i}$ and $\overrightarrow{R}$ the position vectors of the satellite and the receiver respectively:

$$r_i = \hat{r}_i \cdot \overrightarrow{r_i} = \hat{r}_i \cdot \left(\overrightarrow{S_i} - \overrightarrow{R}\right) = \hat{r}_i \cdot \overrightarrow{S_i} - \hat{r}_i \cdot \overrightarrow{R} \tag{22}$$

gives, from (21) and (22):

$$P_i^* = c\Delta_r t + \hat{r}_i \cdot \overrightarrow{S_i} - \hat{r}_i \cdot \overrightarrow{R} \tag{23a}$$

$$\hat{r}_i \cdot \overrightarrow{R} - c\Delta_r t = \hat{r}_i \cdot \overrightarrow{S_i} - P_i^* \tag{23b}$$

Taking $u_{r_i}^x$, $u_{r_i}^y$ and $u_{r_i}^z$ the components of $\hat{r}_i$ gives G the matrix of the geometry of the constellation:

$$G = \begin{pmatrix} u_{r_1}^x & u_{r_1}^y & u_{r_1}^z & -1 \\ \vdots & \vdots & \vdots & \vdots \\ u_{r_n}^x & u_{r_n}^y & u_{r_n}^z & -1 \end{pmatrix} \tag{24}$$

and the matrix notation of Eq. 23b:

$$G\begin{pmatrix} x \\ y \\ z \\ c\Delta_r t \end{pmatrix} = \begin{pmatrix} \hat{r}_1 \cdot \overrightarrow{S_1} - P_1^* \\ \vdots \\ \hat{r}_n \cdot \overrightarrow{S_n} - P_n^* \end{pmatrix} \tag{25}$$

Taking $(G^T G)^{-1}G$ the generalized inverse of G gives the solution of Eq. 25):

$$\begin{pmatrix} x \\ y \\ z \\ c\Delta_r t \end{pmatrix} \simeq (G^T G)^{-1}G\begin{pmatrix} \hat{r}_1 \cdot \overrightarrow{S_1} - P_1^* \\ \vdots \\ \hat{r}_n \cdot \overrightarrow{S_n} - P_n^* \end{pmatrix} \tag{26}$$

One issue remains with the solution given in Eq. 26: three unknowns, x, y and z (the coordinates of the receiver R), are needed to calculate the components of $\hat{r}_i$, on the right side. Iteration is therefore necessary, with a guessed value for $\overrightarrow{R}$ at the start, but with $S_i \gg R$ even large errors on the guessed value of $\overrightarrow{R}$ do not greatly affect the accuracy of $\hat{r}_i$—see Eq. 22—and therefore neither G. It has been found that an error of 200 m on one value of R influences the next value by only about 1 mm. When x, y and z are not known at all, taking 0 as a start value, i.e. $\overrightarrow{R}$ at the center of the Earth, and iterating over Eq. 26 four or five times gives the solution, if there is one, within 1 mm.

If $n > 5$, Eq. 25 is used to check for erroneous pseudo-ranges from the residual. When an erroneous pseudorange is found, it is removed and the calculations redone.

Results

Figure 2 shows an example of a tomographic image over the European region that has been integrated through and contoured to show the spatial distribution of vertical TEC. The example has been chosen arbitrarily and is for 12:00 UT on the 13th October 2002. This shows a gradient in the
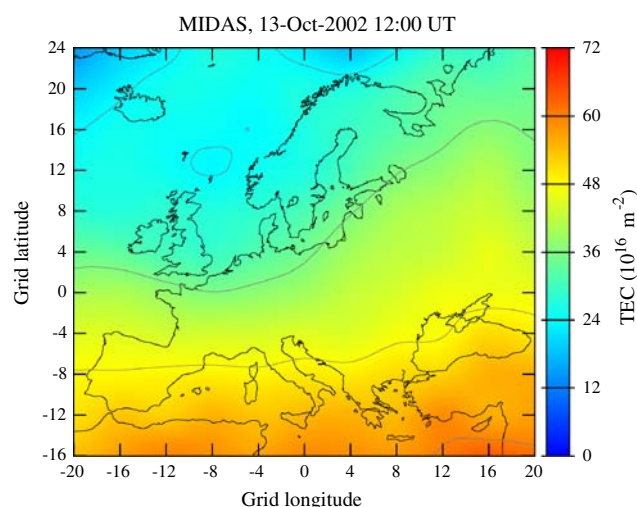

Fig. 2 TEC from the MIDAS image of 13 October 2002 12:00 UT

TEC which increases to the south as would be expected for this time and location.

Figure 3 shows the diurnal variation of the mean vertical (a) and horizontal (b) positioning errors for the receiver at site location GOPE and of their respective 90% percentile, (c) and (d). Each curve shows positioning error calculated on a point-by-point basis then averaged (mean) or sorted (percentile) over all of the points for that hour and for all the days of this study. The general accuracy is, in increasing order: uncorrected, Klobuchar, IRI2001, 40 min forecast, near real-time and dual frequency. It can be seen by comparing (a) with (b) and (c) with (d) that the majority of the positioning error caused by the ionosphere impacts the vertical component rather than the horizontal one.

Figures 4 and 5 show the mean and 90% percentile positioning errors for the four test sites (see Fig. 1) for all the days of this study. All four sites show the same order of increasing accuracy. Comparing the uncorrected results in each of the four graphs (red curve) the largest errors occur at midday, with the most northerly site, MAR6, experiencing mean values of about 10 m (90% 18 m), the middle one, GOPE, mean values of about 11 m (90% 20 m) and the two southerly sites, VILL and ANKR, mean values of about 13 m (90% 20 m). The Klobuchar model reduces these errors to mean values of about 4; 3 and 4 m respectively (90% 10; 9 and 9 m). Interestingly the IRI model is able to bound all of the errors at mean values of about 3 m (90% 6 m). This implies that it is compensating for the ionospheric error for the southerly sites better (in percentage terms) than those to the north. The MIDAS and

Fig. 3 Absolute error components for GOPE : mean vertical (**a**), mean horizontal (**b**), 90% percentile vertical (**c**) and 90% percentile horizontal (**d**)
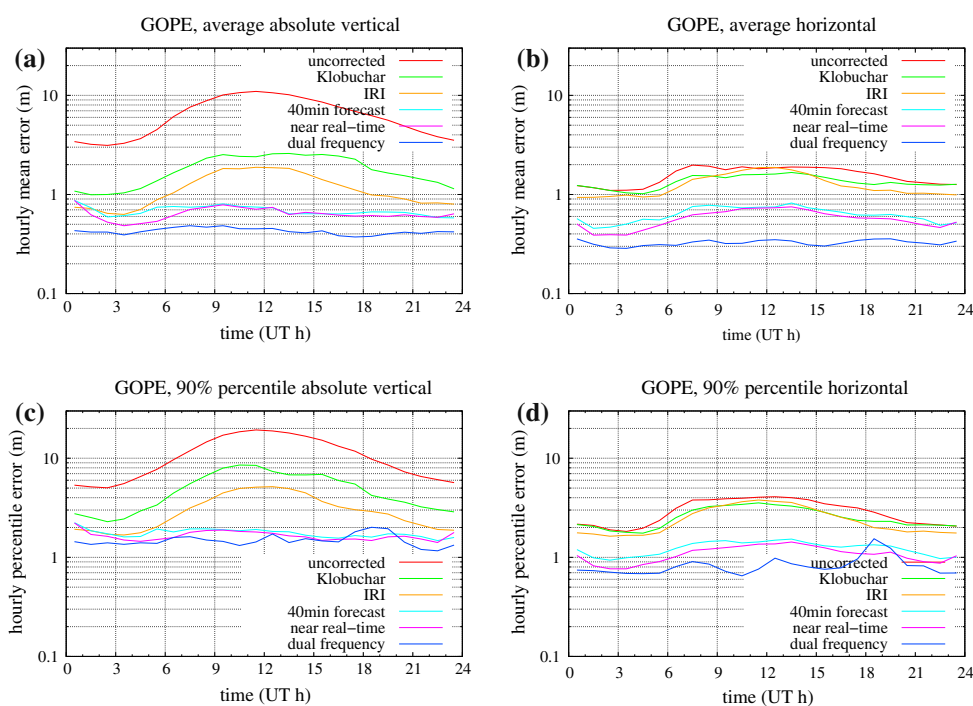
Fig. 4 Average absolute positioning error for MAR6 (**a**), GOPE (**b**), VILL (**c**) and ANKR (**d**)
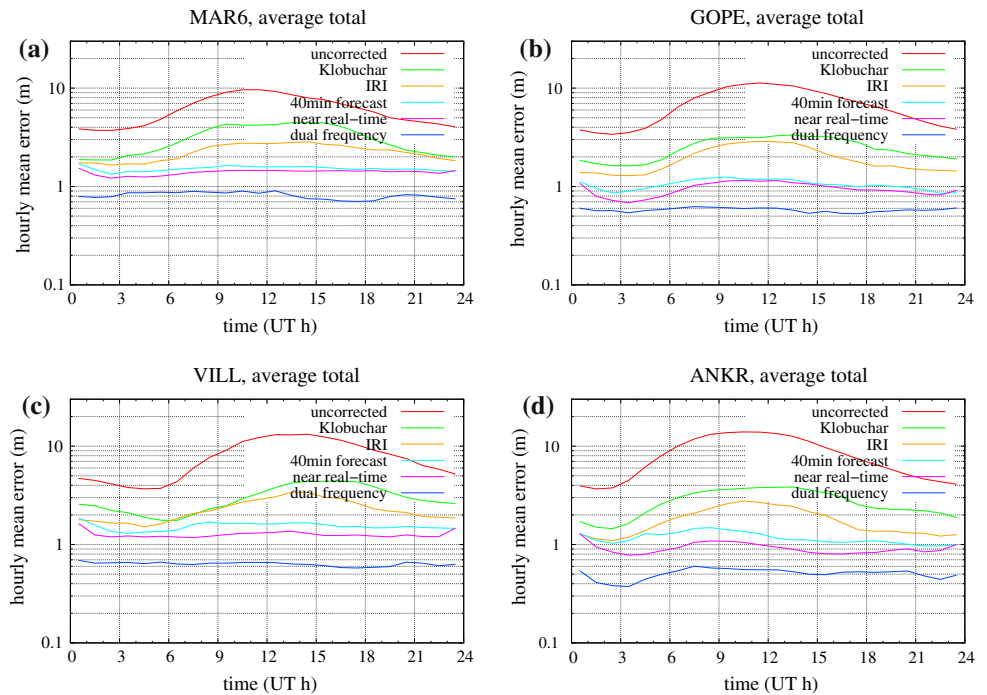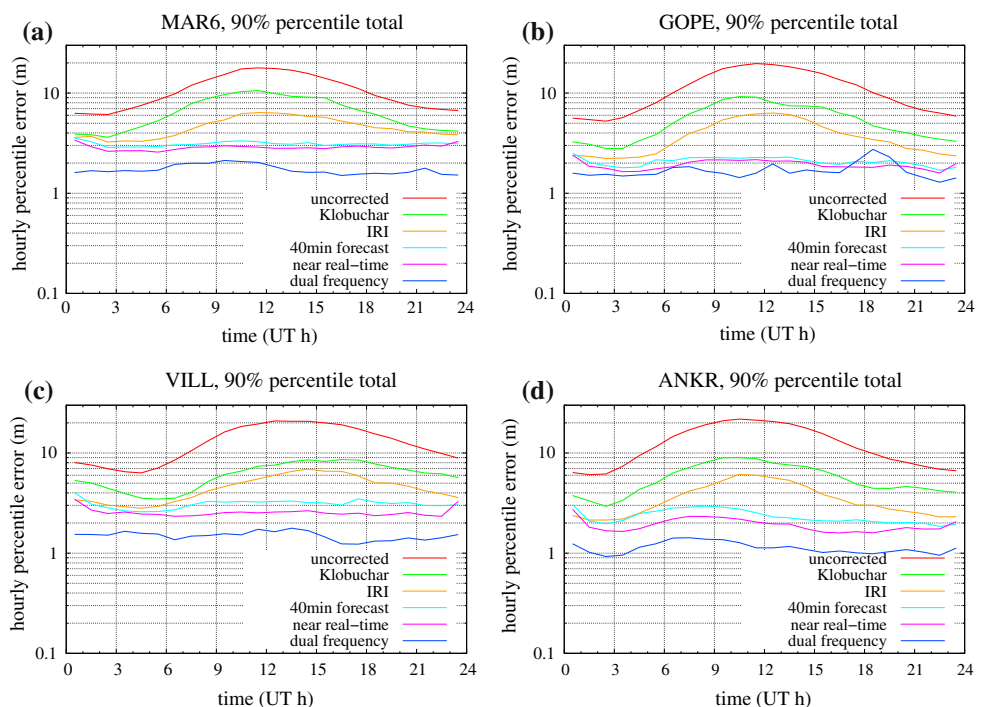

Fig. 5 90% percentile absolute positioning error for MAR6 (**a**), GOPE (**b**), VILL (**c**) and ANKR (**d**)

the 40 minute forecasted MIDAS are able to bound the error at mean values of around 1.5 m (90% 3 m) and the dual frequency receiver at mean values of about 0.5 m (90% 1.5 m) for these real-time positions. MIDAS is noticeably better for GOPE than for the other sites and this is likely to be due to the fact that GOPE is in the center of the image region; thus is it likely that the MIDAS maps are most accurate where the surrounding distribution of

receivers is good. The mean and 90% percentile positioning errors for GOPE are summarized in Table 1.

Figure 6 shows the same as Fig. 4 but for just one day of the study: 13 October 2002. This day was a geomagnetically quiet day with a Kp of 1.0 to 2.7. The hour-to-hour variability of the ionosphere is more apparent here from the uncorrected single frequency positioning errors. The general order of the accuracy is similar to the mean results of

Table 1 Day-time positioning errors (m) for GOPE for all the days of the study

Method	Mean	90% Percentile
Uncorrected	11	20
Klobuchar	3	9
IRI	3	6
MIDAS	1.5	3
Dual frequency	0.5	1.5

Fig. 4. The Klobuchar model performs well on this day and, like IRI, is bounded at about 5 m. MIDAS is bounded at around 3 m.

Figure 7 shows the same as Fig. 6 for another day of the study: 30 October 2003. This day was, over Europe, a negative geomagnetic storm day, which means the ionosphere was greatly depleted. The Kp index was between 4.7 and 9. The uncorrected positioning error is, during the day, about half of its mean value, showing the negative effect of the storm. The Klobuchar model performs very badly on this day, four times worse than its mean value, reaching above 16 m. Comparing the Klobuchar TEC with the MIDAS and the dual-frequency values shows the Klobuchar actually compensated about five times as much as it should have on this day. The general order of the accuracy for IRI, MIDAS and dual-frequency is similar to the mean results of Fig. 4 but there are some points to note. IRI performs almost as well as MIDAS during the day for MAR6, the most northerly station. The signal has suffered from L2 losses of lock on this day and hence the

positioning for the two more northerly sites, MAR6 and GOPE, is sometimes less accurate on the dual frequency result. MIDAS (Fig. 8b) shows there were clusters of strong enhancement over Northern Europe in the evening explaining attenuation of the GPS signal, especially at the lower L2 frequency. In comparison, the IRI model (Fig. 8a) shows an average ionosphere at that time.

Over Europe, the negative storm day of 30 October 2003 was preceded by two days of positive geomagnetic storm, with the Kp index between 3.0 and 4.7 on the 28 (initial phase) and between 4.0 and 9.0 on the 29. MIDAS TEC maps and positioning results at VILL for these two days are shown on Fig. 9. The uncorrected and dual-frequency results are similar to the mean results of Fig. 4. A larger hour-to-hour variability of the ionosphere on the 29 is shown by the uncorrected single frequency positioning errors. Klobuchar, IRI and MIDAS positioning errors are generally twice as high as the mean results. Klobuchar, IRI and 40 min forecast show particularly strong changes (all increases but for Klobuchar on the 28) in positioning error (Fig. 9a) around 11:30 UT on the 28, when the normally equatorial enhancement extended to most of Europe (Fig. 9b), and around 19:30 UT on the 29, when the normally polar depletion extended to most of Europe (Fig. 9c).

Conclusions

In this paper, different methods of correcting for the ionospheric delay have been compared for 4 stations

Fig. 6 Absolute error on the 13 October 2002 for MAR6 (**a**), GOPE (**b**), VILL (**c**) and ANKR (**d**)
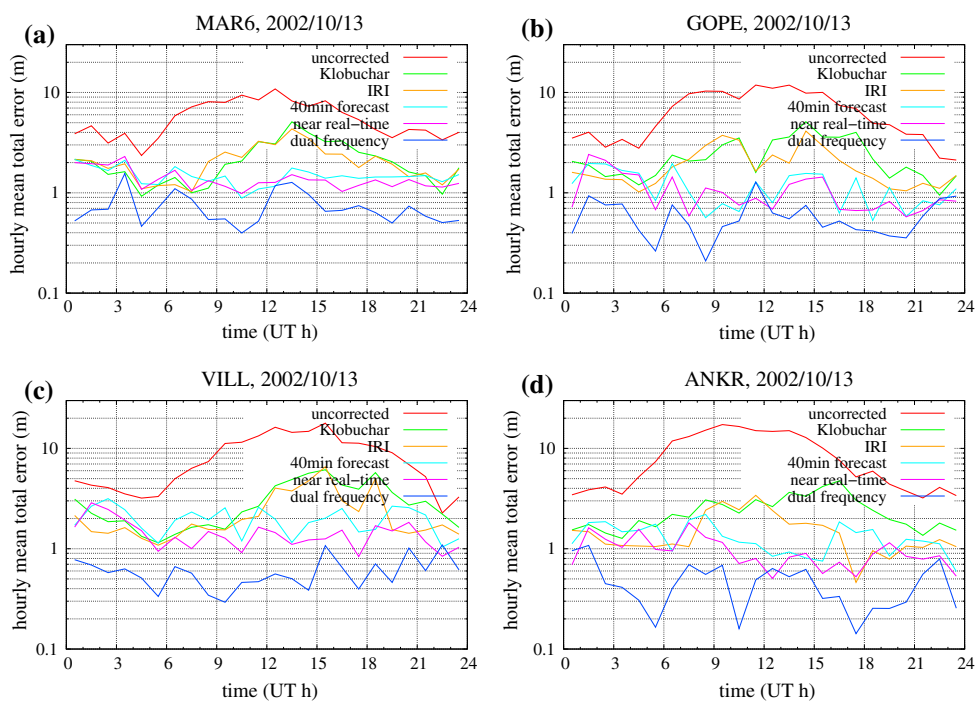
Fig. 7 Absolute error on the 30 October 2003 for MAR6 (**a**), GOPE (**b**), VILL (**c**) and ANKR (**d**)
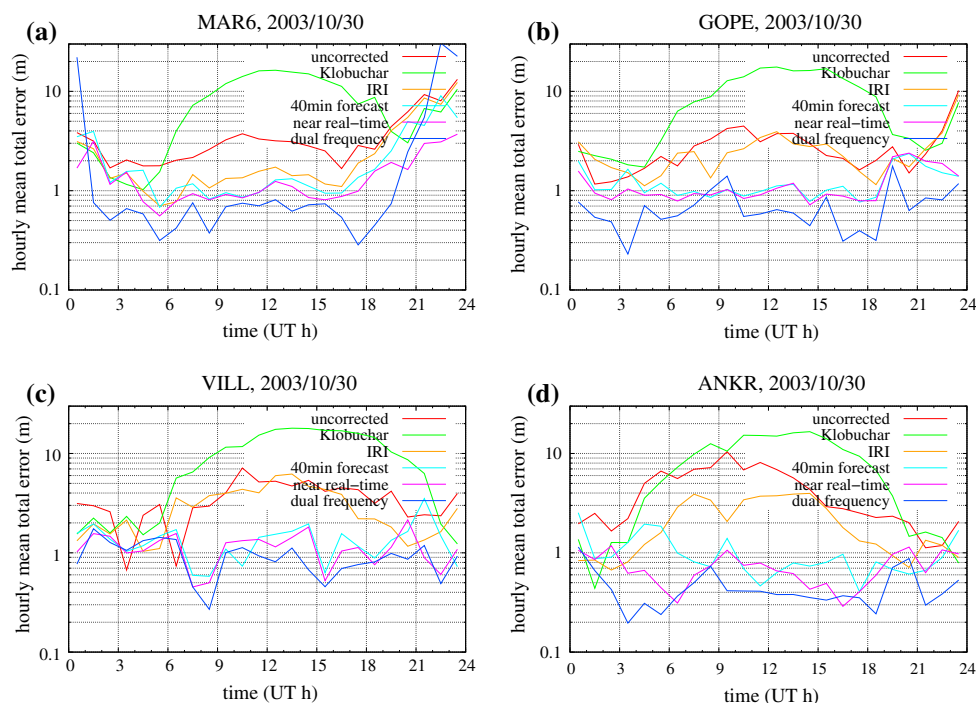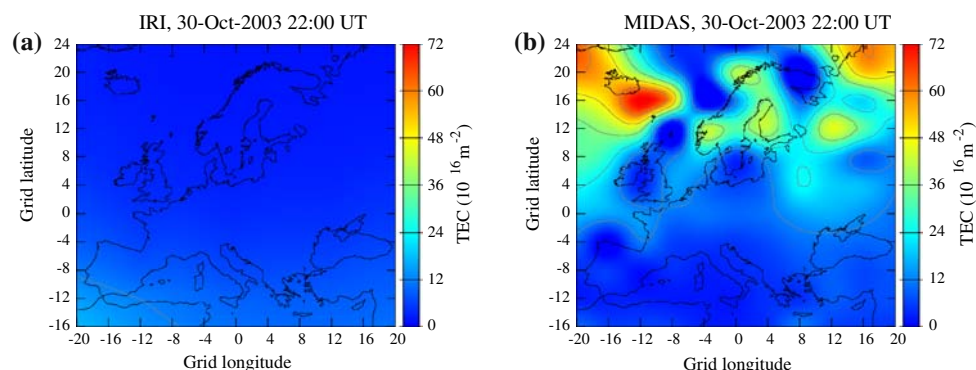

**Fig. 8** TEC from the IRI (**a**) and MIDAS (**b**) images of 30 October 2002 22:00 UT

around the European region in 2002 and 2003. The first method uses no correction; the second and third use respectively the Klobuchar (1987) and International Reference Ionosphere (IRI) models; the fourth and fifth use respectively predicted and near real-time images from a four-dimensional inversion algorithm described by Mitchell and Spencer (2003), called Multi Instrument Data Analysis System (MIDAS); the benchmark uses dual-frequency carrier-smoothed corrections. The results were presented as hourly mean and hourly 90% percentile of the absolute error. It was shown that, while the Klobuchar and IRI models compensate for most of the ionospheric delay, the MIDAS images perform almost as well as the dual-frequency benchmark. Also, most of the positioning error comes from the vertical component. Using MIDAS images gives a position on average within 1.5 m and 90% of the time within 3 m throughout the day, when the values during the day are 4 and 10 m for the Klobuchar model

and 3 and 6 m for the IRI model. The horizontal positioning error is less than 2 m 90% of the time for the station at the center of the map. MIDAS performs well even under extreme storm conditions and sometimes even better than dual-frequency as it is not vulnerable to losses of lock on the L2 frequency. The 40 min predicted MIDAS performs almost as well as the near real-time MIDAS, apart from rare and short periods when the ionosphere is particularly complex and dynamic. The greatest errors appear to be for locations at the outset of the network used for the MIDAS inversion and are probably due to the lower accuracy of the MIDAS images in these areas. The area of this study was generally under the mid-latitude region of the ionosphere. Future work will be carried out for a region under the equatorial anomaly, where the (TEC) is much higher.

This study has shown that, in general, the MIDAS method compensates the ionospheric delay better than the

Fig. 9 Absolute error on the 28 and 29 October 2003 for vill (**a**) and TEC from the MIDAS images of 28 October 2002 11:10 UT (**b**) and of 29 October 2002 19:00 UT (**c**)
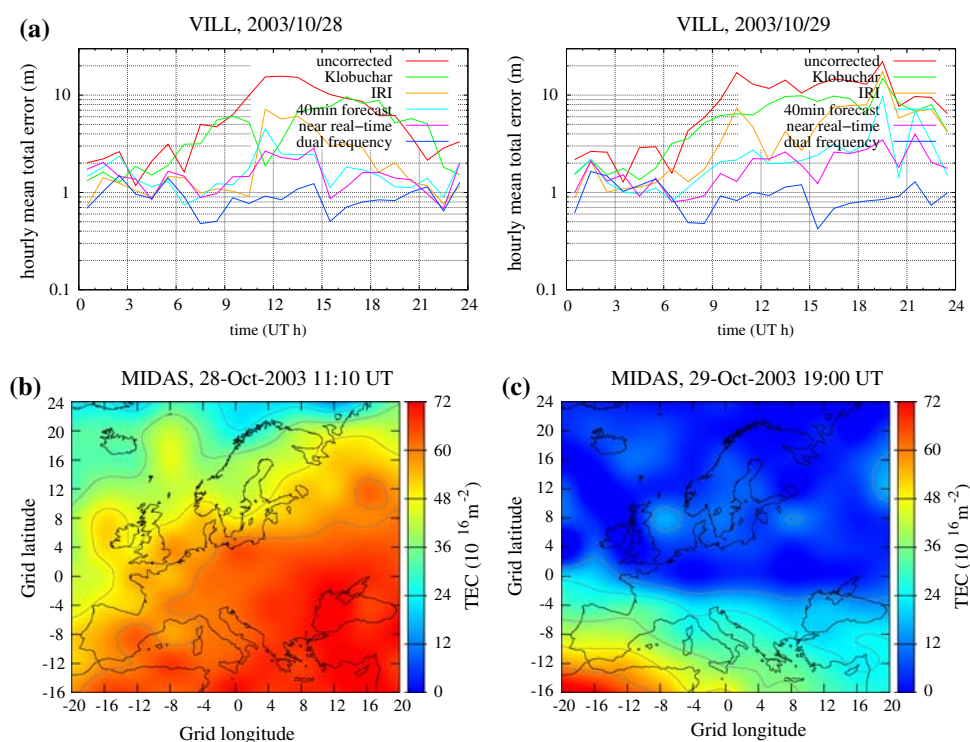
Klobuchar or IRI models. It compensates almost as well as dual-frequency, and sometimes gives an even better positioning as it is not vulnerable to losses of lock.

References

Ashby N, Spilker JJ (1995) Introduction to relativistic effects on the global positioning system. In: Spilker JJ, Parkinson BW (eds) Global positioning system: theory and applications, vol 1. AIAA, pp 623–697

Bilitza D (2001) IRI 2000. Radio Sci 36(2):261–276

Bust GS, Mitchell CN (2008) History, current state, and future directions of ionospheric imaging. Rev Geophys 46

Dear RM (2007) Wide area forecasting of total electron content over europe. PhD Thesis, University of Bath

Dow JM, Neilan RE, Gendt G (2005) The international GPS service: celebrating the 10th anniversary and looking to the next decade. Adv Space Res 36:320–326

Hernández-Pajares M, Juan JM, Sanz J (2000) Application of ionospheric tomography to real-time GPS carrier-phase ambiguities resolution, at scales of 400-1000 km and with high geomagnetic activity. Geophys Res Lett 27:2009–2012

Klobuchar JA (1987) Ionospheric time-delay algorithm for single-frequency gps users. IEEE Trans Aerospace Electron Syst AES 23(3):325–331

Klobuchar JA (1996) Ionospheric effects on GPS. In: Spilker JJ, Parkinson BW (eds) Global positioning system: theory and applications, vol 1. AIAA, pp 485–515

Kouba J, Héroux P (2001) Precise point positioning using IGS orbit and clock products. GPS Solut 5(2):12–28

Mannucci A, Iijima B, Lindqwister U, Pi X, Sparks L, Wilson B (1999) GPS and ionosphere. In: Stone WR (ed) Review of radio science 1996–1999. Oxford University Press, Oxford, pp 625–665

Meggs RW, Mitchell CN (2006) A study into the errors in vertical total electron content mapping using gps data. Radio Sci 41

Mitchell CN, Spencer PSJ (2003) A three dimensional time-dependent algorithm for ionospheric imaging using GPS. Ann Geophys 46(4):687–696

Parkinson BW (1996) GPS error analysis. In: Spilker JJ, Parkinson BW (eds) Global positioning system: theory and applications, vol 1. AIAA, pp 469–483

Schenewerk M (2003) A brief review of basic GPS orbit interpolation strategies. GPS Solut 6(4):265–267

Schmid R, Steigenberger P, Gendt G, Ge M, Rothacher M (2007) Generation of a consistent absolute phase-center correction model for gps receiver and satellite antennas. J Geod 81(12):781–798

Spencer PSJ, Mitchell CN (2007) Imaging of fast moving electron-density structures in the polar cap. Ann Geophys 50(3):427–434

Spilker JJ (1994) Tropospheric effects on GPS. In: Spilker JJ, Parkinson BW (eds) Global positioning system: theory and applications, vol 1. AIAA, pp 517–546

Author Biographies

Damien J. Allain gained his BSc (Hons) in Applied Physics at the University of Central Lancashire in 2002. He then went on to do an

MSc in Hydrography at the University of Plymouth, awarded in 2005. He is currently in the final year of a PhD at the Department of Electronic and Electrical Engineering of the University of Bath, carried out in collaboration with the School of Electronics and Computer Science of the University of Southampton.

Cathryn N. Mitchell researches into the development and application of new algorithms in tomography. She also holds an EPSRC advanced fellowship in the effects of the ionised atmosphere on GNSS. She has published over 50 journal papers including invited review papers in the Proceedings of the Royal Society and in American Geophysical Union journals Space Weather and Reviews of Geophysics. Her group has been awarded a number of prizes for their research in both tomography and GPS. Her current academic position is Professor at the University of Bath where she is director of Invert: Centre for Imaging Science.